

# Polarimetric RCS Prediction Software Code for Large and Complex Objects

Hirokazu Kobayashi, Song Shi, Yoshio Yamaguchi

Dept. of Information Eng., Niigata University, Niigata, Japan

Beijing Municipal Institute of Labor Protection, Beijing, China

Dept. of Information Eng., Niigata University, Niigata, Japan

kobayashi@ie.niigata-u.ac.jp; seki@ast-l.com; yamaguchi@ie.niigata-u.ac.jp

**Abstract-** This paper discusses RCS (Radar Cross Section) predicting software code based on high-frequency technique, Physical Optics (PO) and Physical Theory of Diffraction (PTD) which are powerful asymptotic technique for the surface and edge currents integral in the computation of RCS for large and complex object. By distinguishing between illuminated and un-illuminated areas of target for multiple scattering fields, we can obtain total polarimetric scattering fields of an observation point. Target model is available for not only isolated one but also wide area terrain surface such as ground or sea, with various forms of vegetation, tree, or building. In order to keep high shadowing accuracy, an adaptive subdivision scheme algorithm, which is depending on the situation of incident-, reflection-, scattering-shadowing and multiple reflections, is applied to processing of this distinction. Since both of co- and cross-polarized RCS fields are calculated, the results are useful and effective for studying full polarimetric radar image processing or remote-sensing image decomposition analysis. In this paper we show description of scattering theory for the developed code to calculate full polarimetric RCS and several calculated RCS examples including Doppler spectrum simulation and measurement.

**Keywords-** Polarimetric Radar Cross Section (RCS); Physical Optics (PO); Physical Theory of Diffraction (PTD); Adaptive Shadowing; Systematic Prediction Code; Doppler spectrum

## I. INTRODUCTION

The significance of the RCS in the outcome of radar engagements makes its prediction an important problem in modern systems such as polarimetric Synthetic Aperture Radar (SAR) on space/air-borne for remote-sensing or collision avoidance radar for Intelligent Transfer System (ITS). Many useful techniques have already been developed to provide realistic results. They can be based on exact methods (IE: integral equations, MoM: method of moments, FDTD: finite-difference time-domain, FEM: finite element method and so on [1, 2]) or high-frequency approximate approaches. One can refer to commercial or non-commercial software package such as WIPL-D, FEKO, XFDTD, XPATCH [3] and so on. Generally, most numerical methods are exact but have commonly a drawback to be limited to electrically small size objects.

In this paper, we discuss the systematic software code, which is developed by using typical high-frequency method, namely the Physical Optics (PO) and Physical Theory of Diffraction (PTD), in order to predict the RCS of complex and large targets on or not on wide area such as ground. The PTD is an integrative powerful technique in which the PO uniform current on a discontinuous surface of target is refined by the additional non-uniform component due to the presence of the discontinuity especially such as an edge. The developed code has minimum computer resource requirements and provides convenient run-times.

It utilizes the scientific and engineering computational features of MATLAB and its Graphical User Interface (GUI) functions to provide an error-free encoding of input parameters and efficient calculation. The developed code, named ACES (*Accurate Calculation of Electromagnetic Scattering*), provides many powerful computational capabilities, including the shadowing, the multiple reflections, the approximate effects of the ground and the effects of materials and coatings. Output result of RCS is not only co-polarized but also cross-polarized field. Four powerful engines are developed and embedded in the software. They are Incident Shadowing Engine (ISE), Reflection Shadowing Engine (RSE), Scattering Shadowing Engine (SSE) and Multiple Reflection Engine (MRE). By dynamically re-segmenting the triangular facets according to the situation of shadowing and reflection at the specific angle in the computation process, we can obtain good agreements with measurement.

By employing PTD, the effect of current along edge is also considered in the code. Induced surface current representation can be related to the dynamic re-segmentation of the triangular facets which is depending on the situation of incident, reflection, scattering shadowing and multiple reflections. A user-friendly GUI design of materials database is also developed. A user updateable database of materials and coatings can be applied to models in one or multiple layers, and the computation of their effects on the RCS of models. The user can easily apply the information of material to the computational model and get the information of material which is applied on the computational model interactively.

## II. FORMULATION PO AND PTD BASED ON ELECTROMAGNETIC CURRENTS

The Physical Optics (PO) approximation is one of the most convenient well known RCS prediction methods for an arbitrary 3-dimensional target [4]. The induced currents are integrated over the illuminated portions of the target surface to obtain the scattered far field, while setting the current to zero over the shadowed portions. Thus, the electromagnetic surface currents are given as  $\mathbf{J}_s(\mathbf{r}') = \mathbf{n} \times \mathbf{H}^i$ ,  $\mathbf{M}_s(\mathbf{r}') = \mathbf{E}^i \times \mathbf{n}$  for illuminated region and zero for shadow region, where  $\mathbf{n}$  is the unit normal vector of the surface directed outward and  $\mathbf{H}^i$ ,  $\mathbf{E}^i$  are the incident magnetic and electric field vector respectively. The electric and magnetic surface currents,  $\mathbf{J}_s(\mathbf{r}')$  and  $\mathbf{M}_s(\mathbf{r}')$ , are then used in the radiation integrals to compute the scattered far-field from the target. PO is a high-frequency approximation method that gives best results for electrically large bodies ( $L > 5\lambda$ ,  $\lambda$ : wavelength) and is most accurate in the specular directions. If the source illuminating the target is at a far enough distance, then the incident field can be regarded as a plane wave. PO surface current is integrated over the

illuminated surface of the scatterer. The scattered field component is found by calculating the following integral equation [5],

$$E_{\theta,\phi}^{PO} = -jk \frac{\exp(-jkr)}{4\pi R} \cdot \int_S \{Z_0 \mathbf{J}_s \cdot \mathbf{i}_{\theta,\phi} \pm \mathbf{M}_s \cdot \mathbf{i}_{\phi,\theta}\} \exp(jk\mathbf{r}' \cdot \mathbf{i}_R) ds \quad (1)$$

where  $k = 2\pi/\lambda$ ,  $\lambda$  is the wavelength of the incident wave,  $\mathbf{r}'$  is position vector for the source  $\mathbf{J}_s(\mathbf{r}')$  and  $\mathbf{M}_s(\mathbf{r}')$ ,  $\mathbf{i}_R$  and  $R$  are unit vector and the distance to observation from origin,  $Z_0 = \sqrt{\mu_0/\epsilon_0}$  is free space impedance,  $(\mathbf{i}_\theta, \mathbf{i}_\phi)$  are the unit vectors of the spherical coordinate system, and  $(E_\theta^{PO}, E_\phi^{PO})$  are the scattered electric field components which are evaluated over a lit region  $S$  in the spherical coordinates. Equation (1) is for co-polarized field and by exchanging  $\mathbf{i}_\theta$  and  $\mathbf{i}_\phi$ , cross-polarized field can be obtained.

For a case of non-metal flat plate, we can more explicitly derive a following reduced expression from the proposing Formula (1).

$$E_{\theta,\phi}^{PO} = -jk \frac{\exp(-jkr)}{4\pi R} D_{\theta,\phi} \int_S \exp\{-jk(\mathbf{k}^i - \mathbf{k}^s) \cdot \mathbf{r}'\} dS' \quad (2)$$

$$D_\theta = E_1 \{(1 + R_\parallel) \cos \theta - (1 - R_\parallel) \cos \theta_0\} \cos(\phi_0 - \phi) - E_2 \{(1 - R_\perp) \cos \theta_0 \cos \theta - (1 + R_\perp) \sin(\phi_0 - \phi)\},$$

$$D_\phi = E_1 \{(1 + R_\parallel) - (1 - R_\parallel) \cos \theta_0 \cos \theta\} \sin(\phi_0 - \phi) + E_2 \{(1 - R_\perp) \cos \theta_0 + (1 + R_\perp) \cos \theta\} \cos(\phi_0 - \phi),$$

where  $E_1$  and  $E_2$  are amplitudes of the incident wave given as  $\mathbf{E}^i = \{E_1 \mathbf{i}_\theta + E_2 \mathbf{i}_\phi\} \exp(jk\mathbf{k}^i \cdot \mathbf{r})$ ,  $\mathbf{k}^i$  and  $\mathbf{k}^s$  are wave-number vector of incident and scattered wave, and  $R_\parallel$  and  $R_\perp$  are parallel and perpendicular coefficients of reflected wave, respectively, as discussed below. Judgment for lit or shadow region can be processed by using formula  $\mathbf{k}^i \cdot \mathbf{n} < 0$ , which is an illuminated case. The incident angle  $(\theta_0, \phi_0)$  and the observation angle  $(\theta, \phi)$  are independent each other. For  $\theta$ -polarized (TM-wave) or  $\phi$ -polarized (TE-wave), amplitude of incident wave  $E_2$  or  $E_1$  becomes to be zero, respectively. In case of  $E_1 = E_2$ , polarization of scattered field becomes to be slanted 45 degree from the unit vector  $\mathbf{i}_\theta$  and  $\mathbf{i}_\phi$ .

When a body is illuminated by a plane wave, current is induced on its surface. Around the edges of the body, this current has more complicated behavior, due to the diffraction of the incident field. The edge diffracted field appears to come from a non-uniform line source located at the edge. Concept of PTD method is an idea to consider this non-uniform current into PO additionally. According to the PTD or the method of equivalent currents, any finite current distribution yields a finite result for the far-zone diffracted field. The diffracted field  $\mathbf{E}^d$  due to an edge discontinuity  $C$  is given for far zones by the radiation integral as equivalent edge currents [6, 7],

$$\mathbf{E}^d = -jk \oint_C \{Z_0 \mathbf{i}_r \times \mathbf{i}_t \times \mathbf{i}_t I_l^{nu}(\mathbf{l}') + \mathbf{i}_r \times \mathbf{i}_t M_l^{nu}(\mathbf{l}')\} \cdot \frac{\exp(-jkr)}{4\pi r} d\mathbf{l}' \quad (3)$$

where, as shown in Figure 1,  $\mathbf{i}_t$  is tangential unit vector of the edge,  $I_l^{nu}(\mathbf{l}')$  and  $M_l^{nu}(\mathbf{l}')$  are equivalent electromagnetic edge

currents along edge length  $\mathbf{l}'$ , and  $r$  is distance between observation and the edge of target. Then the total scattered fields of PTD can be represented as  $\mathbf{E}^S = \mathbf{E}^{PO} + \mathbf{E}^d$ .

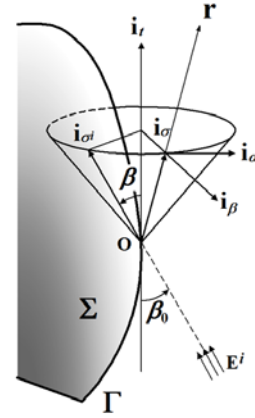


Figure 1: Diffraction by a wedge and equivalent current along the edge.

### III. MULTIPLE REFLECTION SCHEME FOR CURVED IMPEDANCE SURFACE

Multiple reflection is considered that a reflected plane wave, which illuminates to an impedance plane # $m$ , again incidents to an impedance plane # $m+1$ . Regarding as subscript  $(m)$  means plate number and  $R_\parallel(m)$ ,  $R_\perp(m)$  are reflection coefficient for parallel  $\theta$ - (TM-wave) and perpendicular  $\phi$ -polarization (TE-wave), respectively, of plate # $m$ , relating expressions are

$$\mathbf{E}_{(m)}^i = P_{(m)}^i \mathbf{T}_{(m)}^i + Q_{(m)}^i \mathbf{B}_{(m)}, \quad (4a)$$

$$\mathbf{E}_{(m)}^r = R_\parallel(m) P_{(m)}^i \mathbf{T}_{(m)}^r + R_\perp(m) Q_{(m)}^i \mathbf{B}_{(m)}, \quad (4b)$$

$$\mathbf{B}_{(m)} = \frac{\mathbf{k}_{(m)}^i \times \mathbf{n}_{(m)}}{\sin \theta_{(m)}^i} = \frac{\mathbf{k}_{(m)}^r \times \mathbf{n}_{(m)}}{\sin \theta_{(m)}^r}, \quad (4c)$$

$$\mathbf{T}_{(m+1)}^{i,r} = \mathbf{B}_{(m)} \times \mathbf{k}_{(m)}^{i,r}, \quad (4d)$$

$$\mathbf{k}_{(m)}^r = \mathbf{k}_{(m)}^i - 2\mathbf{n}_{(m)}[\mathbf{n}_{(m)} \cdot \mathbf{k}_{(m)}^i] \quad (4e)$$

where subscripts  $i, r$  are meaning to incident and reflected wave, respectively,  $P^{i,r}$ ,  $Q^{i,r}$  are amplitude and phase variable of geometrical wave. Expressing wave-number unit vector of incident and reflected wave are  $\mathbf{k}^i$ ,  $\mathbf{k}^r$  (or  $\mathbf{k}_i$ ,  $\mathbf{k}_r$  in Figure 2 and 3) respectively, then a vector  $\mathbf{B}$  vertical to incident plane is defined as  $\mathbf{B} = \mathbf{k}^i \times \mathbf{n} / \sin \theta_0 = \mathbf{k}^r \times \mathbf{n} / \sin \theta_0$ , and  $\theta_0$  is an angle between  $\mathbf{k}^i$  and  $\mathbf{n}$  as shown in Figure 2. The vector  $\mathbf{k}^i$  and  $\mathbf{k}^r$  are determined by the law of Snell,  $\mathbf{k}^r = \mathbf{k}^i - 2\mathbf{n}(\mathbf{n} \cdot \mathbf{k}^i)$ . A vector  $\mathbf{T}^{i,r}$  can be defined as  $\mathbf{T}^{i,r} = \mathbf{B} \times \mathbf{k}^{i,r}$ .

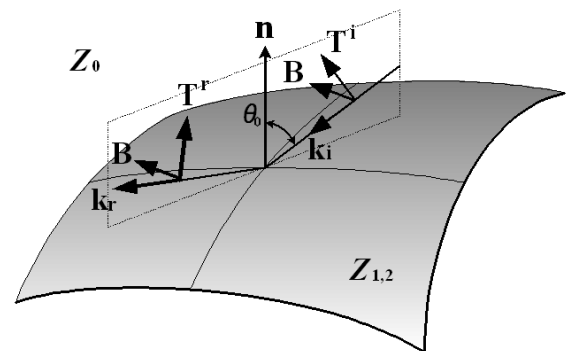


Figure 2: Geometrical wave reflection from curved impedance surface.

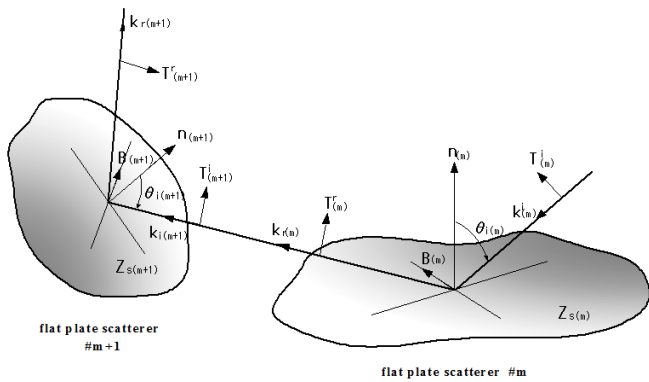


Figure 3: Multiple reflections among impedance surfaces.

Thus, wave number vector of reflected wave at a plane  $\#m$ ,  $\mathbf{k}_{(m)}^r$ , equals to  $\mathbf{k}_{(m+1)}^i$  which is one of incident wave at a plane  $\#m+1$ . In general  $\mathbf{B}_{(m)}$  and  $\mathbf{B}_{(m+1)}$ ,  $\mathbf{T}_{(m)}^{i,r}$  and  $\mathbf{T}_{(m+1)}^{i,r}$  are not equal, as shown in Figure 3. So, if relative geometrical position relation of a plane  $\#m$  and  $\#m+1$  is once obtained, explicit expression can be expanded, especially normal vector relation of each plane is most important. In this situation, we can get a following relation [8],

$$\mathbf{B}_{(m+1)} = \frac{\mathbf{k}_{(m)}^r \times \mathbf{n}_{(m+1)}}{\sin \theta_{(m+1)}^i}, \quad (5a)$$

$$\mathbf{T}_{(m+1)}^i = \frac{\mathbf{n}_{(m+1)} - [\mathbf{k}_{(m)}^r \cdot \mathbf{n}_{(m+1)}] \mathbf{k}_{(m)}^r}{\sin \theta_{(m+1)}^i}, \quad (5b)$$

$$\mathbf{T}_{(m+1)}^r = \frac{[1 - 2(\mathbf{k}_{(m)}^r \cdot \mathbf{n}_{(m+1)})] \mathbf{n}_{(m+1)} + \{\mathbf{k}_{(m)}^r \cdot \mathbf{n}_{(m+1)}\} \mathbf{k}_{(m)}^r}{\sin \theta_{(m+1)}^i}. \quad (5c)$$

#### IV. REFLECTION AND REFRACTION COEFFICIENTS OF MULTILAYERED DIELECTRIC SHEETS

In this section, we discuss reflection and refraction from multiple layered dielectric flat sheets, as shown in Figure 4. For scattering by a target which has dielectric portions, introducing boundary condition of surface impedance makes easy to formulate electromagnetic relations. On the other hand, we can also obtain exact general formulation for this model such a multiple layered dielectric sheets which is infinitely flat. As a result, the coefficients of reflection and refraction obtained from the solution of wave equation are exactly formulated by characteristic matrix of dielectric permittivity, magnetic permeability and thickness of each dielectric sheet. And we can calculate the coefficients from metal backed sheets by infinite permittivity of a sheet and dielectric loss by considering complex permittivity [9].

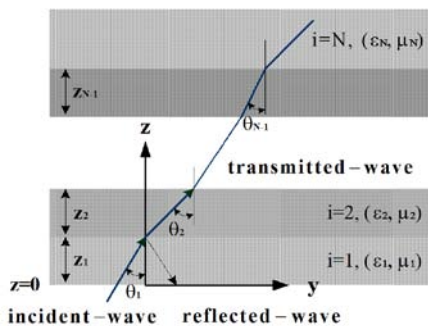


Figure 4: Multiple reflections between impedance flat planes

Now as shown Figure 4, N-layered sheets with infinite length to y-axis are overlapped along z-axis. Incident angle is  $\theta_{i=1}$  measured from normal z-axis of a first sheet,  $\epsilon_i$  and  $\mu_i$  ( $i = 1 \sim N$ ) are permittivity and permeability, respectively, which are function of variable z. In case TE-wave, electric field vector is perpendicular to incident plane, components y, z of the field are 0, and then only a group of ( $E_x, H_y, H_z$ ) remains. Concentrating to electrical field component,  $E_x$ , Maxwell's equation reduces to 3-equations,  $\frac{\partial E_x}{\partial z} + j\omega\mu H_y = 0$ ,  $\frac{\partial E_x}{\partial y} - j\omega\mu H_z = 0$ ,  $\frac{\partial H_z}{\partial y} - \frac{\partial H_y}{\partial z} - j\omega\epsilon E_x = 0$ . Assuming permeability depends on  $\mu = \mu(z)$  and noting  $\frac{\partial(\mu H_y)}{\partial z} = H_y \frac{d\mu}{dz} + \mu \frac{\partial H_y}{\partial z}$ , we can obtain following basic equation

$$\left\{ \frac{\partial^2}{\partial y^2} + \frac{\partial^2}{\partial z^2} + n^2 k^2 \right\} E_x = -j\omega H_y \frac{d\mu}{dz} = \frac{\partial(\log \mu)}{\partial z} \frac{\partial E_x}{\partial z} \quad (6)$$

where  $\omega^2 \epsilon \mu = n^2 k^2$ . After some calculation, for example using variable separation method, following characteristic matrix for a dielectric sheet is obtained [9].

$$M(\xi, \varphi) = \begin{pmatrix} \cos \varphi & -\frac{j}{\xi} \sin \varphi \\ j\xi \sin \varphi & \cos \varphi \end{pmatrix}, \quad (7a)$$

$$\varphi = nkz \cos \theta, \quad \xi = \begin{cases} \sqrt{\epsilon_r/\mu_r} \cos \theta & \text{TE-wave} \\ \sqrt{\mu_r/\epsilon_r} \cos \theta & \text{TM-wave} \end{cases}. \quad (7b)$$

Letting the thickness of each sheet is  $z_i$  ( $i = 1 \sim N$ ), each characteristic matrix is recurrently obtained as  $i = 1: G_0 = M_1 G(z_1)$ ,  $i = 2: G(z_1) = M_2 G(z_2)$ ,  $\dots$ . Therefore, the matrix of the sheets  $i = 1$  to  $N$  is

$$G_0 = M_1 G(z_1) = M_1 M_2 G(z_2) = \dots = M_1 M_2 \dots M_N G(z_N) = M(z_N) G(z_N). \quad (8)$$

The relation between the matrix elements and coefficients can be derived as follow. Regarding incident angle of first ( $i = 1$ ) and last boundary as  $\theta_1$  and  $\theta_N$ , and amplitude of incident, reflected and refracted wave as  $A_i, A_r$ , and  $A_t$ , reflection and refraction coefficient are defined to  $R = A_r/A_i$  and  $T = A_t/A_i$ , respectively. As  $m_{ij}$  are the 4 elements of matrix  $M$ , and considering the constraint condition  $A_i + A_r = (m_{11} + m_{12}\xi_N)A_t$  and  $\xi_1(A_i - A_r) = (m_{21} + m_{22}\xi_N)A_t$ , the coefficients are lastly obtained as

$$R = \frac{A_r}{A_i} = \frac{m_{11}\xi_1 - m_{12}\xi_1\xi_N - m_{21} - m_{22}\xi_N}{m_{11}\xi_1 - m_{12}\xi_1\xi_N + m_{21} + m_{22}\xi_N}, \quad (9a)$$

$$T = \frac{A_t}{A_i} = \frac{2\xi_1}{m_{11}\xi_1 + m_{12}\xi_1\xi_N + m_{21} + m_{22}\xi_N}. \quad (9b)$$

For example  $N = 3$ , let first and third sheet are free space and permittivity and permeability of second ( $i = 2$ ) sheet are  $\epsilon_2, \mu_2$ , respectively. For this case, the characteristic matrix is calculated as

$$m_{11} = m_{22} = \cos \varphi, m_{12} = j \frac{1}{\xi_2} \sin \varphi, m_{21} = j \xi_2 \sin \varphi, \quad \varphi = n_2 k z_2 \cos \theta_2, \quad \xi_2 = n_2 \cos \theta_2. \quad (10)$$

Therefore putting  $i = 3$  into previous equation, the coefficients are obtained as

$$R = \frac{R_{12} + R_{23} \exp[i\varphi - j2\varphi]}{1 + R_{12} + R_{23} \exp[i\varphi - j2\varphi]}, \quad (11a)$$

$$T = \frac{T_{12} T_{23} \exp[i\varphi - j\varphi]}{1 + T_{12} T_{23} \exp[i\varphi - j2\varphi]}, \quad (11b)$$

$$R_{12} = \frac{\xi_1 - \xi_2}{\xi_1 + \xi_2} = \frac{n_1 \cos \theta_1 - n_2 \cos \theta_2}{n_1 \cos \theta_1 + n_2 \cos \theta_2}, \quad (11c)$$

$$R_{23} = \frac{\xi_2 - \xi_3}{\xi_2 + \xi_3} = \frac{n_2 \cos \theta_2 - n_3 \cos \theta_3}{n_2 \cos \theta_2 + n_3 \cos \theta_3}, \quad (11d)$$

$$T_{12} = \frac{2\xi_1}{\xi_1 + \xi_2} = \frac{2n_1 \cos \theta_1}{n_1 \cos \theta_1 + n_2 \cos \theta_2}, \quad (11e)$$

$$T_{23} = \frac{2\xi_2}{\xi_2 + \xi_3} = \frac{2n_2 \cos \theta_2}{n_2 \cos \theta_2 + n_3 \cos \theta_3}, \quad (11f)$$

where  $n_{1,2} = \sqrt{\epsilon_{r(1),r(2)}/\mu_{r(1),r(2)}}$  for TE-wave. As expected, these coefficients are a single dielectric sheet and perfectly agree with Fresnel formula.

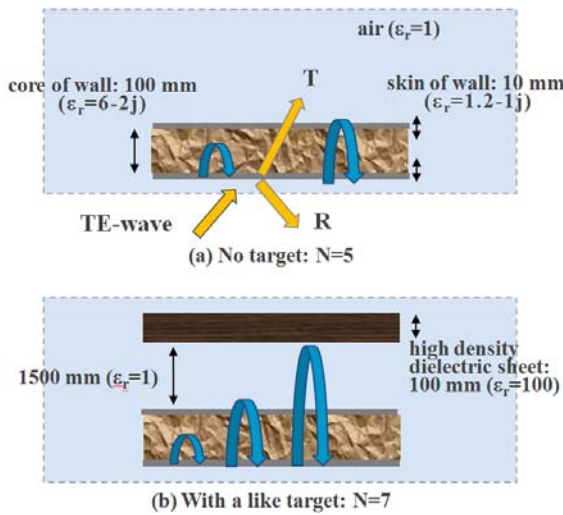


Figure 5: Multiple reflection application for wall-through-radar.

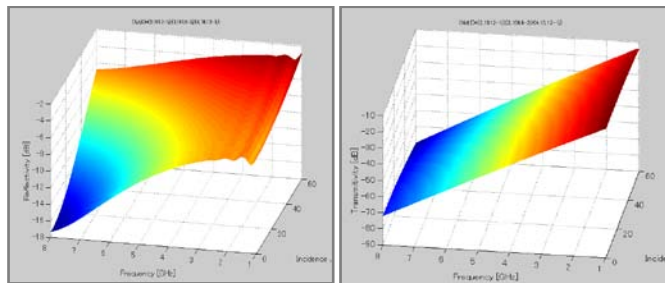


Figure 6: Reflection (Left) and transmission (Right) coefficients with no high density dielectric (metal-like target) sheet.

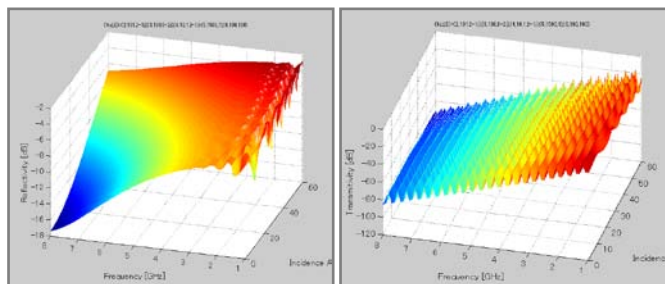


Figure 7: Reflection (L) and transmission (R) coefficients with high density dielectric (metal-like target) sheet on the same condition of Figure 6.

Next we show an interesting and simple example for a like wall-through-radar indicated in Figure 5 configuration which is 7-layer dielectric sheets. The wall is constructed by 3-sheets, namely 2- skins and one core. The radar target is high density dielectric or metal sheet separated 1.5m from the wall. Free space (air) is assigned to 1st, 5th and 7th sheet. Figure 6 is reflection and transmission coefficients calculated by Equation (8) with no radar target (metal-like dielectric sheet) and Figure 7 is with the sheet. The frequency range is 1-8 GHz, the incident angle is 0 ~ 60 degree and the vertical axis is the calculated coefficient including its loss causing by complex permittivity (relative permeability  $\mu_r = 1$ ). Difference between Figure 6 and 7 is due to the high density sheet, and frequency response in low band especially is changed and rippled signs appear according with incident angle.

Generally, most of actual objects are made from various metallic and/or non-metallic materials. Consequently the general and systematic code is indeed necessary in order to predict characteristics of target RCS. According this novel idea of multiple reflections and these non-metallic multi-sheets, one can estimate scattering fields by complex objects with refracting wave like radome. It may be available for microwave remote-sensing application as fully polarimetric components regarding objects such as sea or ground as a single sheet with deep thickness. These coefficients for multiple layers can be also applied to design radome or radio absorption material.

## V. ADAPTIVE SUBDIVISION SCHEME

The object surface of computational model consists of triangular facets. When shadowing or multiple reflections occurs on the triangular facets, only a part of the triangular facets that being illuminated by the incident or reflected wave have a contribution to the scattering field. We propose an adaptive subdivision new scheme to cope with this situation.

At each specific incident angle or reflection angle, the coordinate of the triangular facets is transferred to a new coordinate that the z-coordinate is along with the direction of the incident or reflected electric wave. Then, all triangular facets of the model are projected onto the new xy-plane. The overlapped part between the current triangular facet and the projected facet is subtracted from the current facet and the current facet is subdivided into 3 triangular new facets in this case as shown in Figure 8. The contribution to the scattering field by the current triangular facet is re-organized as the contribution by the 3 newly generated triangular facets. Each engine, namely ISE, RSE, SSE and MRE, employs the adaptive subdivision scheme to cope with the shadowing.

Shadowing example for a square trihedral corner with a sphere is shown in Figure 9 and 10. The former is a case of no processing and the latter is shadow processing current intensity distribution at incident angle  $\theta_0 = 55^\circ, \phi = 45^\circ$  degrees. The contribution to the scattering field by the current triangular facet is reorganized as the contribution by the three triangular facets. This adaptive subdivision processing is applied to the each engine including Scattering Shadowing Engine and Multiple Reflection Engine of the developed code.

In "Configure/Calculation" menu in the ACES opening window, the GUI consists of five modules: Mono-static RCS versus angle, Mono-static RCS versus frequency, Bi-static RCS versus angle, Bi-static RCS versus frequency and Induced current. In Figure 11, for reference, the simulation parameters of the developed code for mono-static RCS

calculation are displayed. The incident wave operates at frequency of 10GHz and its polarization is in  $\theta$ -direction. For simple the material of the calculated model and the ground is PEC (perfecting electrical conductor). Incident Shadowing and Multiple Reflection are also considered. Figure 12 is outline of the developed code configuration and calculating flow.

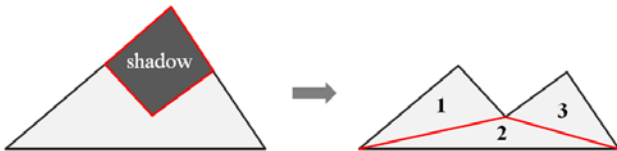


Figure 8: Adaptive shadowing in subdivision processing.

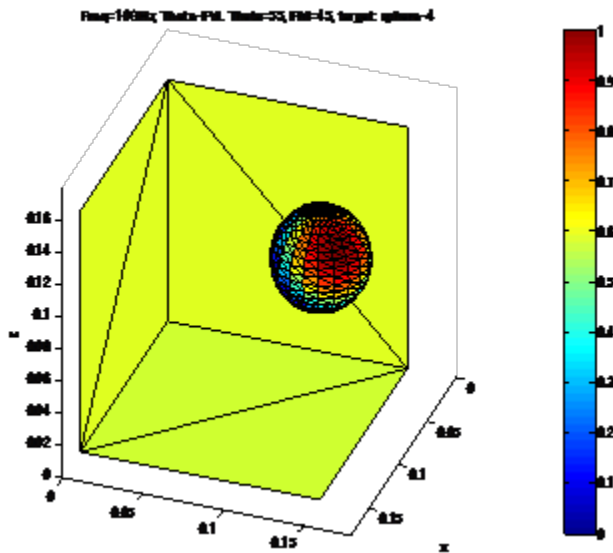


Figure 9: Surface current distribution without shadowing on a square trihedral corner with a sphere (incident angle  $\theta_0 = 55^\circ, \phi = 45^\circ$ ).

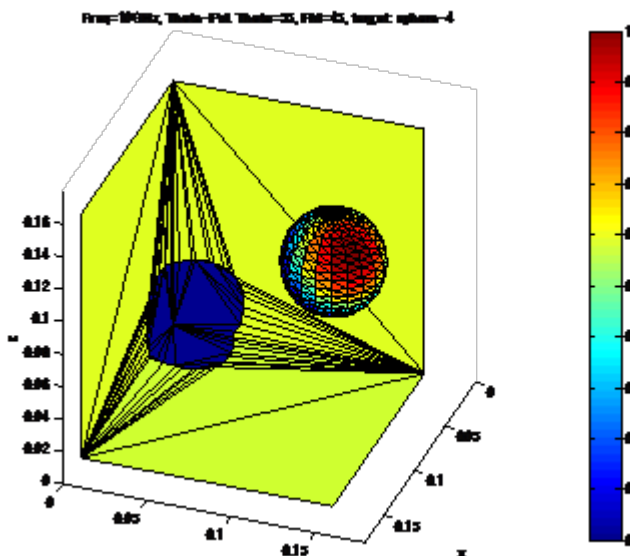


Figure 10: Surface current distribution with shadowing on a square trihedral corner with a sphere (incident angle  $\theta_0 = 55^\circ, \phi = 45^\circ$ ).

## VI. SOME SIMULATION RESULTS TO RCS AND DOPPLER ESTIMATION

This section presents a RCS simulation example of airplane as shown in Figure 13 and a large tree on wide area ground, and Doppler spectrum simulation of a helicopter using the

developed software code, which is available to calculate and estimate complex and large radar target with/-out wide area like ground or sea. The code can also calculate full polarimetric fields. Using this code, RCS of corner reflector already verified to moment method and they coincide with each other within  $\pm 0.5$  dB [9].

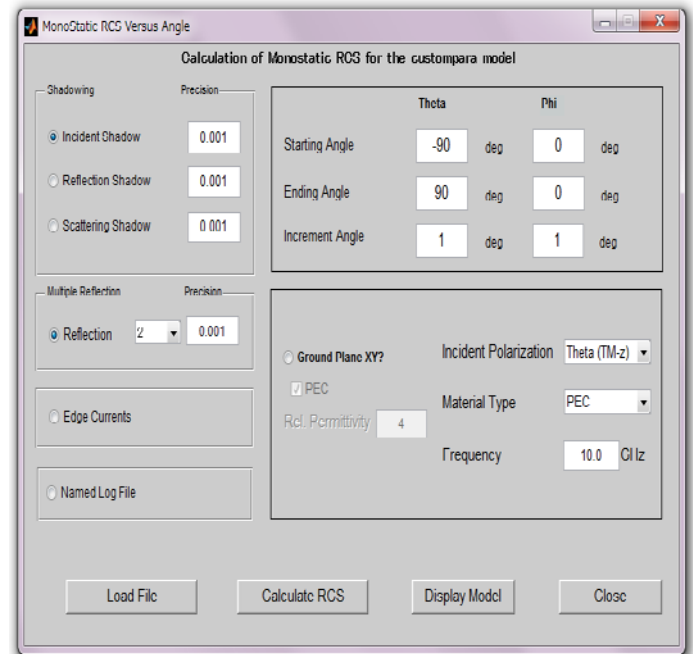


Figure 11: Mono-static RCS calculation parameters in the developed code.

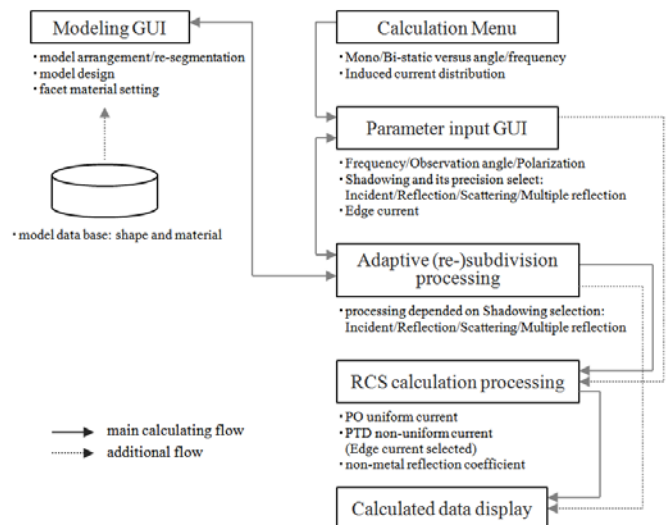


Figure 12: Outline of ACES configuration and calculating flow.

As shown in Figure 13, for the airplane, the x-, y-, and z-dimension are 9.9m, 6.0m, and 2.0m, respectively, and z-coordinate range is 10m. Figure 14 shows the polar plot of monostatic RCS at 10GHz without ground plane. We can see from the Figure that cross-polarized component of RCS is comparatively high level in a half space, 180 ~ 360 degree (rear area of the airplane) because the airplane has twisting facets to incident field vector direction.

In radar remote-sensing field, analysis of SAR image by full polarimetric information is now in progress [10]. Image of



SAR or Inverse SAR can be regarded as spatial infinitesimal variation of the electromagnetic field, so SAR simulation and general radar signal processing like clutter suppression or Doppler spectrum become to be available by this code.

Figure 15 and 16 show surface current distribution on a large tree ( $h = 10\text{m}$ ) illuminated by 10GHz plane wave and mono-static co/cross-polar pattern which are  $\theta(V)$ -polarized, respectively. The ground ( $50 \times 50\text{m}^2$ ,  $\epsilon_r = 5 + j0.5$ ,  $\mu_r = 1$ ) with the electrically large tree ( $h \approx 3,333\lambda$ ) is non-metallic model. Figure 16 is co/cross-polarized RCS patterns for horizontal ground plane whose reflection coefficient is calculated by taking the thickness of first sheet over  $h \approx 1,000\lambda$  according to the previous discussion and we can find cross-polarized field components around  $\pm 60 \sim \pm 80$  degree according to the tree branch. If off-nadir angle of SAR is around 30 degree, this model RCS,  $\sigma$ , is a value at  $\theta = \pm 30$  degree. Additionally speaking, there is need in future, to simulate taking account of normalized RCS per unit area or beam width of SAR antenna, surface terrain, shape and permittivity of trees, and some verification with other code or experimental comparison etc.

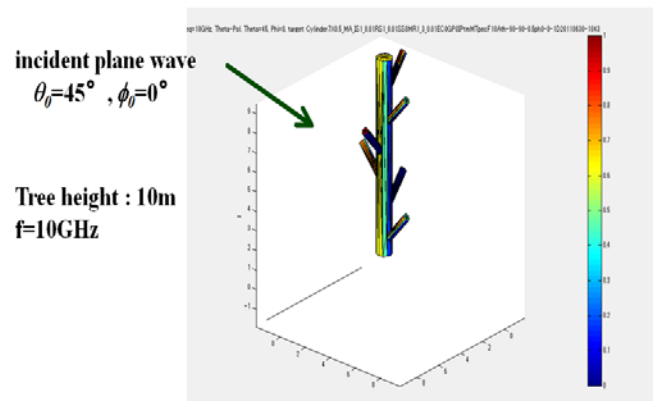


Figure 15: Tree model on a wide ground and surface current.

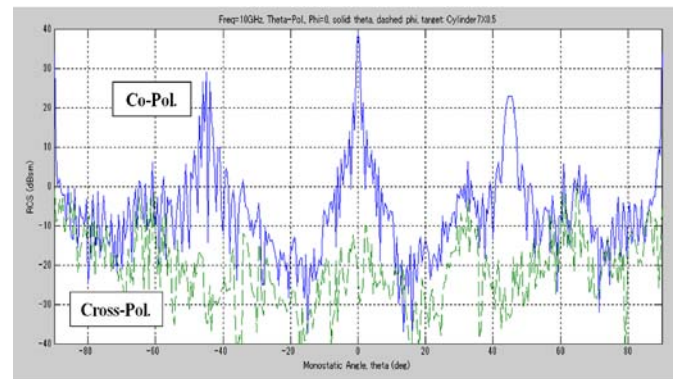


Figure 16: Co/cross-polarized RCS pattern for the model in Figure 15.

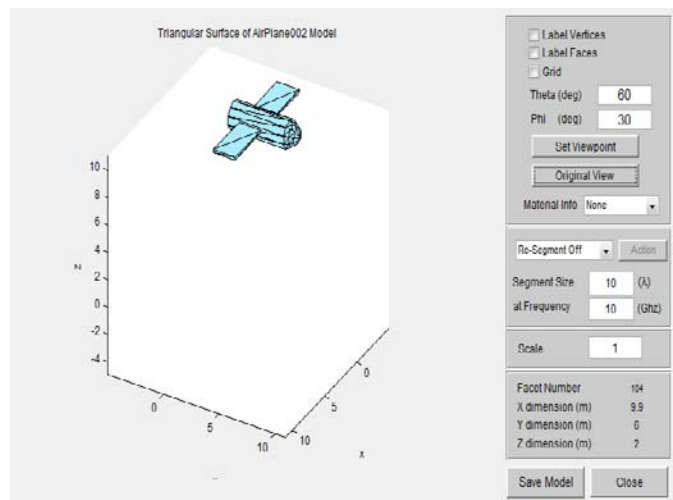


Figure 13: Airplane model developed in the ACES Code.

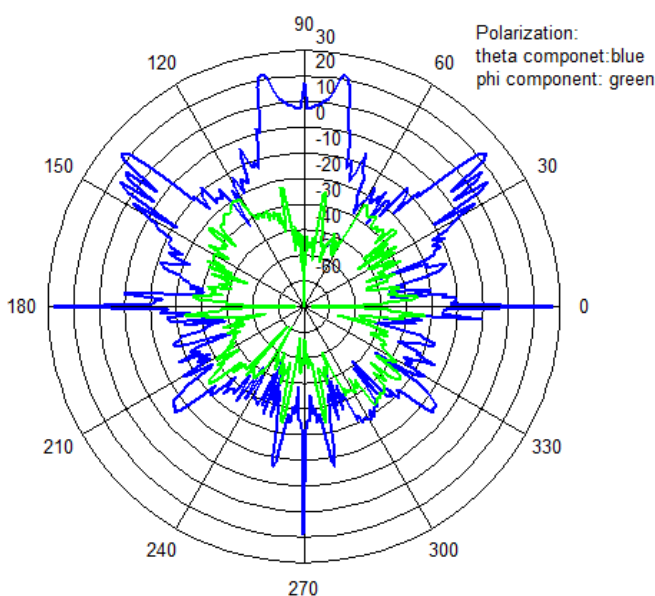


Figure 14: Monostatic RCS polar plot at 10GHz, polarized VV ( $\theta\theta$ ) and cross-polarized VH ( $\theta\phi$ ) for the airplane model in Fig. 12.

Lastly we show a dynamic simulation example for Doppler estimation. Figure 17 is a model for helicopter with 4-main rotors to use in the developed code. The diameter of main and tail rotor is 16.4m and 4.7m, respectively, and rotational speed at its edge is 216 and 121 m/s. Then each rotational number and periodic cycle is 4.2 round/s and 8.4 round/s, and 14.4 kHz and 8.1 kHz. If PRF (pulse repetition frequency) of radar transmitted pulse is 50 kHz, sampling of this model simulation should be fitted to this PRF. In this situation, rotating main and tail rotors and calculating of the whole helicopter under condition of hovering in the code, we obtain simulated results shown in Figure 18 to 20. Figure 18 is RCS change with respect to time (rotation). The RCS amplitude around center is not so changed and caused by body area of the helicopter and high level amplitude is by 4-main rotors which peak are occurred per 0.24/4s because of 4-rotors  $1/4.2=0.24\text{s}$ . Figure 19 is spectrum processed by short time FFT (Fast Fourier Transformation) of data in Figure 18. Figure 20 also is processed in short time (512 points). From Figure 20, we can see locus of the main rotor with maximum level 14.4 kHz which is mentioned as the round cycle of the main rotor.

Furthermore in order to verify the above simulation we measured Doppler spectrum using X-band pulse Doppler radar. The radar target is an actual helicopter which shape is like the model in Figure 17. Figure 21 and 22 are processed data of the measurement as same parameters without incident angle in Figure 19 and 20, respectively. This elevation angle from a ground at the measurement is 20 ~ 30 degree. This difference of incident angle affect to the mismatch around zero-Doppler spectrum of these Figures. And, unfortunately, non-linear devices like a RF amplifier in the radar are not taken into

account to the simulation and IF band of the radar receiver is within 15 kHz because of its low pass filter.

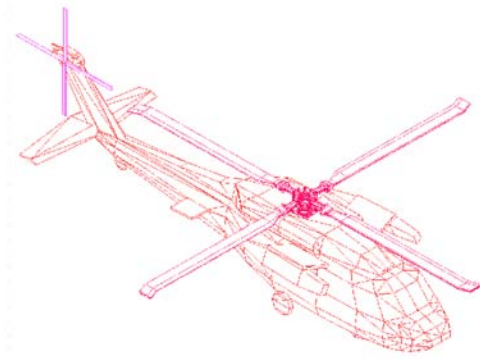


Figure 17: Helicopter simulation model with 4 main rotors.

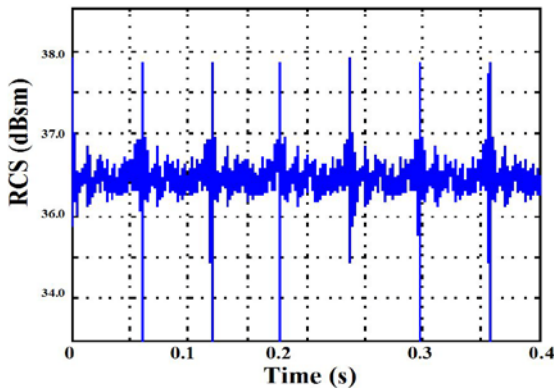


Figure 18: Time variance of simulated RCS at 10 GHz at normal incidence to nose of the model in Figure 17.

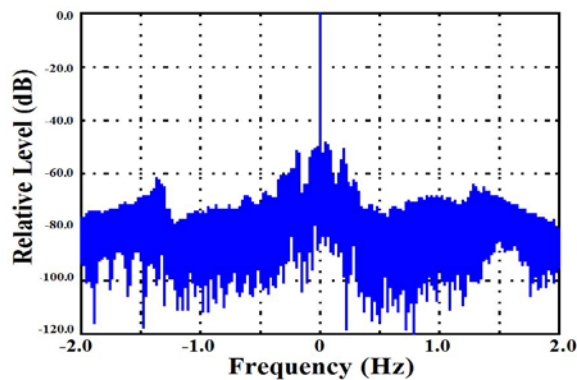


Figure 19: Simulated Doppler spectrum using Figure 18.

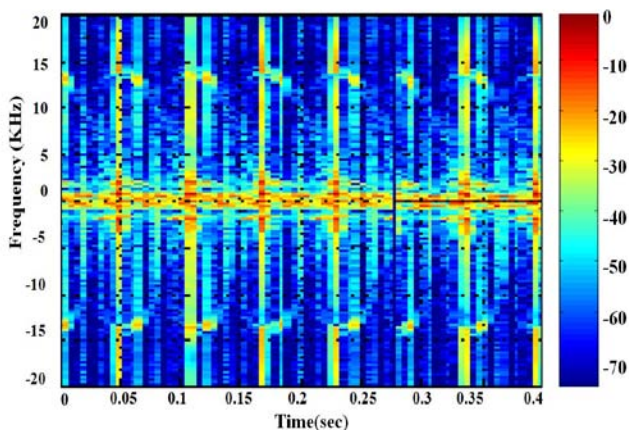


Figure 20: Simulated Short-time spectrum using Figure 18.

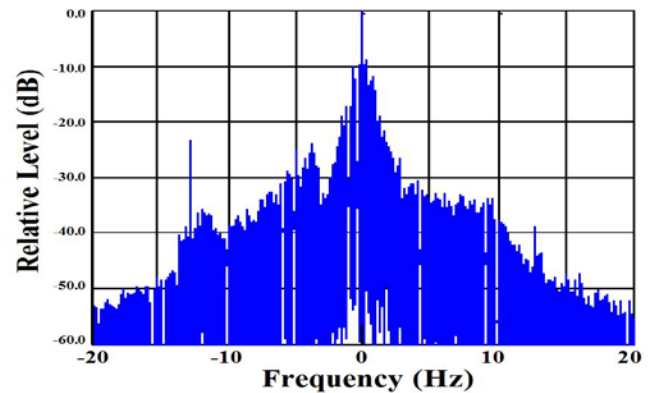


Figure 21: Measured Doppler spectrum by using the pulse Doppler radar: Range/div is different from Figure 19.

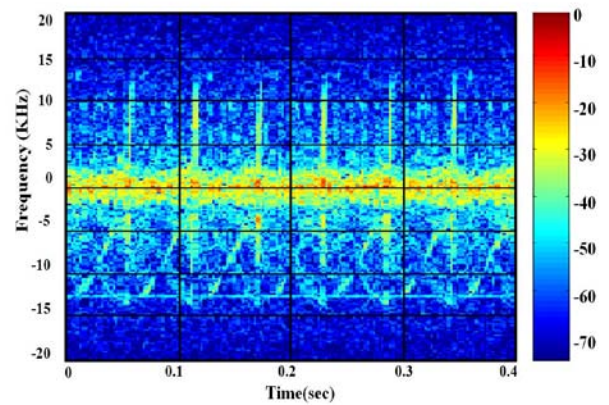


Figure 22: Measured short-time spectrum using Figure 21.

## VII. CONCLUSION

In this paper, consciously considering large and complex object with non-metal portion and semi-infinite space like sea or ground, we proposed the systematic RCS prediction code using accurate high-frequency asymptotic methods, PO and PTD which are based on electromagnetic surface and edge currents. Moreover the code can calculate cross-polarized field for full polarimetric analysis of radar remote-sensing imaging and decomposition. For complex shape objects, software code has to treat not only first reflection but also secondary reflection and diffraction. From this reason, algorithm of shadowing is always necessary. For full polarized RCS, the developed code has an optimum processing unit engine adaptively to treat re-meshing, recurrently calculating unit for multi-layered dielectric sheets and multiple scattering which described in this paper. The trial version of this developed code is available to download from URL [11].

Additionally, we indicated a dynamic simulation example, Doppler analysis using this developed code, and then verified it with measurement data of an actual helicopter by the Doppler radar. These Doppler processing and analysis technology can directly be applied to NCTR (Non Co-operative Target Recognition).

## REFERENCES

- [1] Radar cross section of complex objects, Annals of Telecommunications, vol.50, no.5-6, pp.471-598, 1995.
- [2] D. C. Jenn, Radar and Laser Cross Section Engineering, 2nd ed., IAA Inc., Washington DC, 2005.
- [3] M. Hazlett, D. Andersh and S. W. Lee, "XPATCH: A High Frequency Electromagnetic Scattering Prediction Code Using Shooting and Bouncing Rays," SPIE, vol. 2469, pp.266-275, 1999.

- [4] P. Ya Ufimtsev, Fundamentals of the Physical Theory of Diffraction, IEEE Press, 2007.
- [5] H. Kobayashi, K. Hongo and I. Tanaka, "Expressions of Physical Optics Integral for Smooth Conducting Scatterers Approximated by Quadratic Surfaces," Electronics and Communications in Japan : Part 1, John Wiley & Sons, New York, vol.83, no.7, pp.61-70, July 2000.
- [6] A. Michaeli, "Asymptotic analysis of edge-excited currents on a convex face of a perfectly conducting wedge under overlapping penumbra region condition," IEEE Trans. on Antennas and Propagation, vol.44, no.9, pp.97-101, 1996.
- [7] H. Kobayashi and K. Hongo, "Scattering of Electromagnetic Plane Waves by Conducting Plates," Electromagnetics, vol.17, no.6, pp.573-587, Nov.-Dec. 1997.
- [8] H. Kobayashi, T. Moriyama and K. Hongo, "RCS of Trihedral Corner-reflector with Surface Impedance," IEICE General Conference 2000, B-1-45, March 2000 (in Japanese).
- [9] H. Kobayashi, Electromagnetic Wave in Space, Press-Media, Niigata, Japan, 2011 (in Japanese).
- [10] S. R. Cloude, Polarization: applications in remote sensing, Oxford Univ. Press, 2010.
- [11] <http://www.ast-l.com/Products/>



**Hirokazu Kobayashi** was born in Hokkaido, Japan. He received the B.E.E. and M.E.E. degrees from the Shizuoka University, Shizuoka, Japan in 1978, 1980, respectively, and received the Dr. Eng. degree from Tsukuba University, Tsukuba, Japan, in 2000.

He joined Fujitsu LTD., Kawasaki, Japan at 1980. Since 1981 he has been with the Fujitsu System Integration Laboratories as a Researcher for developments of micro- and millimeter-wave wide-band antennas and passive devices, active phased array radar, and electromagnetic theoretical investigation for scattering cross-sections. During 1999-2010, he served as a Director and General Manager of the Laboratories and Fujitsu LTD. In 2010 he joined the Faculty of Engineering as a Professor in Niigata University, Niigata, Japan. His current research interests are high-frequency electromagnetic analysis for computing of radar cross section of large objects, near-field analysis and imaging using PO/PTD/GTD, and near-field RCS transformation to far-field based on microwave imaging theory such as SAR and Inverse SAR.

Dr. Kobayashi is a Senior member, Antenna and Propagation Society, IEEE, and a member of the Institute of Electronics, Information and Communication Engineers, Japan. He was Adjunct Lecturer of Tsukuba University (2002-2004) and Tokyo Metropolitan University, Advanced Institute of Industrial Technology (2009-2010) and recently he published a book, "Electromagnetic Wave in Space," Press-Media, Niigata, Japan (2011, in Japanese).



**Song Shi** was born in Mudanjiang, China. He received the B.S. and M.S. degrees in physics from Jilin University, Changchun, China, in 1984, 1987 respectively, and the PhD degree in electrical engineering from the University of Tsukuba, Tsukuba, Japan, in 2000.

He was with the China Computer Software and Technology Service Corp. (CS&S) from 1987 to 1992, where he was a Software Engineer in 1990. From 1993 to 1995, he was a System Engineer at Unix System Technology Corp. (USTC). From 1995 to 2000, he was at the Institute of Information Sciences and Electronics, University of Tsukuba, Tsukuba, Japan. From 2000 to 2004, he was a Senior Research Engineer of Mobile Communication at the KDDI Research & Development Laboratories, Inc., Japan. From 2004 to 2009, he was a Senior R&D Engineer at the CTECH Corp., Japan. From 2009 to 2011, he was a CTO at the AST Corp., Japan. Currently, he is a Director of the Electromagnetic Lab at the Beijing Municipal Institute of Labor Protection, China. His interests include mobile communications, smart antennas, circularly polarized antennas, shadowing, reflection and scattering features analysis of electromagnetic wave and high-frequency analysis for the computing of radar cross-section of large objects.



**Yoshio Yamaguchi** received the B. E. degree in electronics engineering from Niigata University, Niigata, Japan, and the M. E. and Dr. Eng. degrees from the Tokyo Institute of Technology, Tokyo, Japan, in 1976, 1978, and 1983, respectively.

In 1978, he joined the Faculty of Engineering, Niigata University, where he is a Professor and Head of the Information Engineering Department. From 1988 to 1989, he was a Research Associate at the University of Illinois at Chicago. His interests are in the field of radar polarimetry, microwave sensing, and imaging.

Dr. Yamaguchi was Chair of the IEEE Geoscience and Remote Sensing Society Japan Chapter (2002-2003), Vice Chair (2000-2001), organizer of Polarimetric Synthetic Aperture Radar Work-shops (2000-2005) in Japan, and Associate Editor for Asian affairs of the GRSS Newsletter since 2003. He is a Fellow of the Institute of Electronics, Information and Communication Engineers, Japan, and was the recipient of the 2008 IEEE GRSS Education Award.